Transient natural convection flows around a thin fin on the sidewall of a differentially heated cavity

FENG XU†, JOHN C. PATTERSON AND CHENGWANG LEI

School of Engineering, James Cook University, Townsville, QLD 4811, Australia

Transient natural convection flows around a thin fin on the sidewall of a differentially heated cavity, which includes a lower intrusion under the fin, a starting plume bypassing the fin and a thermal flow entrained into the vertical thermal boundary layer downstream of the fin in a typical case, are investigated using a scaling analysis and direct numerical simulations. The obtained scaling relations show that the thickness and velocity of the transient natural convection flows around the fin are determined by different dynamic and energy balances, which can be either a buoyancy-viscous balance or a buoyancy-inertial balance, depending on the Rayleigh number, the Prandtl number and the fin length. A time scale of the transition from a buoyancy-viscous flow regime to a buoyancy-inertial flow regime is obtained. The major scaling relations quantifying the transient natural convection flows are also validated by direct numerical simulations. In general, there is a good agreement between the scaling predictions and the corresponding numerical results.

1. Introduction

Transient natural convection flows in a cavity are common in industrial applications such as heat exchangers, solar collectors and nuclear reactors. Understanding of these transient natural convection flows is also of fundamental interest in the fluid mechanics community due to their relevance to fluid mechanics problems over a wide range of scales. A wide literature on transient natural convection has been reported over the past three decades (see e.g. Patterson & Imberger 1980; Ostrach 1988; Hyun 1994).

Previous studies (see e.g. Patterson & Imberger 1980) have shown that following sudden heating, a vertical thermal boundary layer forms adjacent to the sidewall of a differentially heated cavity and the ceiling of the cavity forces a horizontal intrusion flow underneath the ceiling. The vertical thermal boundary layer has received considerable attention since it produces a thermal force to drive natural convection flows in the cavity (see e.g. Elder 1965a, 1965b; Gill 1966). Fundamental scaling relations to characterize the velocity and thickness of the vertical thermal boundary layer and the transition time from an unsteady state to a steady state were also obtained by Patterson & Imberger (1980), some of which were confirmed by experimental measurements (e.g. Xu, Patterson & Lei 2005). Further studies of the scaling relations of the thermal boundary layer were carried out recently by Lin, Armfield & Patterson (2007) and Lin et al. (2009), who also considered the Prandtl number dependence. Moreover, it is found that for the case of sudden heating,

† Present address: School of Civil Engineering, The University of Sydney, Sydney, NSW 2006, Australia. Email address for correspondence: f.xu@usyd.edu.au

perturbations, which are referred to as leading-edge effect (LEE), arise in the vicinity of the leading edge of the vertical thermal boundary layer and propagate downstream (see e.g. Goldstein & Briggs 1964; Mahajan & Gebhart 1978; Joshi & Gebhart 1987; Armfield & Patterson 1992; Patterson *et al.* 2002).

Apart from producing the thermal force, the state of the vertical thermal boundary layer in different flow regimes determines the heat transfer rate through the differentially heated cavity. Accordingly, it is of practical significance for industrial applications to manipulate the flow regimes of the vertical thermal boundary layer. A simple passive approach to alter the vertical thermal boundary layer flow is to place a fin on the sidewall, and thus the study of the natural convection flows around a fin has been extensively reported in the literature over the past three decades (see e.g. Bejan 1983; Oosthuizen & Paul 1985; Shi & Khodadadi 2003; Xu, Patterson & Lei 2006, 2008, 2009).

It is expected that a conducting fin attached to the sidewall increases the surface area of heat transfer and, in turn, increases the overall heat transfer through the cavity (see e.g. Frederick & Valencia 1989; Nag, Sarkar & Sastri 1994; Shi & Khodadadi 2003; Tasnim & Collins 2004; Bilgen 2005). On the other hand, an adiabatic fin may also have a significant impact on natural convection flows in a differentially heated cavity and the heat transfer rate through the cavity (see e.g. Shakerin, Bohn & Loehrke 1988; Nag, Sarkar & Sastri 1993). In the previous studies (e.g. Bilgen 2005), the fin thickness is usually considered to be negligibly small (a so-called thin fin) in comparison with the fin length, and it has also been demonstrated that natural convection flows in the cavity are sensitive to the fin length. Secondary circulations may be observed if the fin length is sufficiently large, and multiple circulations induced by the fin arise at the upper and lower base corners of the fin (Nag *et al.* 1993).

A survey of relevant literature reveals that steady natural convection induced by a fin on the sidewall of a differentially heated cavity has been paid considerable attention, but few studies have focused on the transient natural convection flows around the fin. In many applications, however, the thermal forcing is unsteady and the transient flow response is also of interest. In order to investigate the effect of an adiabatic fin on the transient natural convection flows, the authors have recently carried out a series of experimental measurements and numerical simulations of the transient natural convection flows around an adiabatic fin (see Xu *et al.* 2006, 2008, 2009). Both the experimental and numerical results of Xu *et al.* (2008, 2009) show that, following sudden heating of the sidewall, the early-stage vertical thermal boundary layer flow is separated into two distinct sections if the fin length is greater than the thickness of the vertical thermal boundary layer. The fin and the ceiling of the cavity both force horizontal intrusions. After the lower intrusion under the fin bypasses the fin, a starting plume forms, which ascends until it strikes the intrusion under the ceiling. As time increases further, the starting plume is eventually drawn into the vertical thermal boundary layer downstream of the fin, and a horizontal thermal flow forms above the fin with an adverse temperature gradient (which is potentially unstable, see Xu *et al.* 2009).

It has been demonstrated that an adiabatic fin may change the transient development of the thermal boundary layer flows adjacent to the sidewall and even trigger instability, significantly enhancing the heat transfer rate through the sidewall (by up to 23% in the early stage of the flow development for a Rayleigh number of the order of 10^9; refer to Xu *et al.* 2009). Therefore, it is of fundamental significance to quantify the transient natural convection flows in order to obtain further insights into their dynamic mechanisms in different flow regimes. In this

$$u = v = 0, \frac{\partial T}{\partial y} = 0$$

$u = v = 0,$

$T = T_0 - \Delta T$

l

y

x

Fin

h

$u = v = 0,$

$T = T_0 - \Delta T$

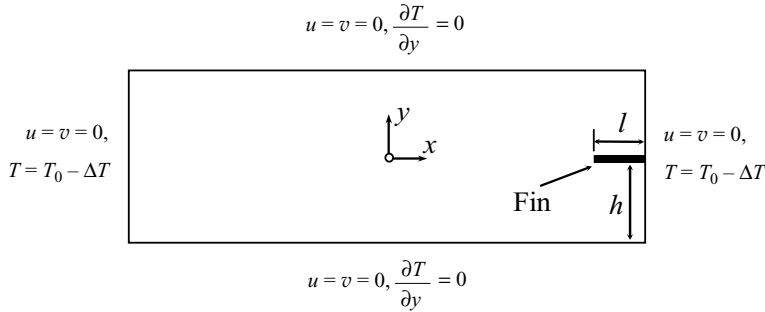$$u = v = 0, \frac{\partial T}{\partial y} = 0$$

FIGURE 1. Schematic of the physical domain and boundary conditions.

paper, a scaling analysis of the early transient natural convection flows around an adiabatic fin is described, following procedures outlined in the previous studies of the transient natural convection flows in a rectangular cavity (Patterson & Imberger 1980; Lin, Armfield & Patterson 2007), in an attic space (Poulikakos & Bejan 1983) and in a wedge-shaped triangular cavity (Lei & Patterson 2002). Note that the dynamic mechanisms of the early transient natural convection flows around the fin are the focus of this study, rather than the steady state that evolves over a long time scale. Corresponding numerical simulations are used to validate the scaling relations obtained from the scaling analysis.

In the remainder of this paper, a scaling analysis of the transient natural convection flows around the fin with a Prandtl number larger than unity is described in §2. The numerical procedures are described in §3. Validation of the scaling relations and further discussion are given in §4, and the conclusions are summarized in §5.

2. Scaling relations of the transient natural convection flows around a thin fin

The comparisons between the experiment and corresponding two-dimensional numerical simulations reported by Xu *et al.* (2009) show that the two-dimensional laminar model characterizes well the early transient flows around the fin for a Rayleigh number up to an order of 10^9. Accordingly, based on the experimental model adopted by Xu *et al.* (2008, 2009), we consider a two-dimensional cavity of H (height) $\times L$ (length) with an adiabatic thin fin (length $l \gg$ thickness d) placed at the mid height of the sidewall (the height of the cavity under the fin is $h = H/2$). The top and bottom walls of the cavity and the fin surfaces are assumed to be adiabatic. The boundary conditions are illustrated in figure 1. Initially the contained fluid is isothermal at a temperature T_0 and stationary. At initiation, the temperature of the finned sidewall is suddenly raised by ΔT and that of the other sidewall is lowered by ΔT. The subsequent development of the working fluid in the cavity is governed by the following Navier–Stokes and energy equations with the Boussinesq approximation:

$$\frac{\partial u}{\partial x} + \frac{\partial v}{\partial y} = 0, \tag{1}$$

$$\frac{\partial u}{\partial t} + u \frac{\partial u}{\partial x} + v \frac{\partial u}{\partial y} = -\frac{1}{\rho} \frac{\partial p}{\partial x} + \nu \left(\frac{\partial^2 u}{\partial x^2} + \frac{\partial^2 u}{\partial y^2} \right), \tag{2}$$

$$\frac{\partial v}{\partial t} + u \frac{\partial v}{\partial x} + v \frac{\partial v}{\partial y} = -\frac{1}{\rho} \frac{\partial p}{\partial y} + \nu \left(\frac{\partial^2 v}{\partial x^2} + \frac{\partial^2 v}{\partial y^2} \right) + g\beta (T - T_0), \tag{3}$$

$$\frac{\partial T}{\partial t} + u \frac{\partial T}{\partial x} + v \frac{\partial T}{\partial y} = \kappa \left(\frac{\partial^2 T}{\partial x^2} + \frac{\partial^2 T}{\partial y^2} \right), \tag{4}$$

where x and y are the horizontal and vertical coordinates with origin at the centre of the cavity, t is the time, T is the temperature, p is the pressure, u and v are the velocity components in the x and y directions, g is the acceleration due to gravity, β is the coefficient of thermal expansion, ρ is the density, κ is the thermal diffusivity and ν is the kinematic viscosity.

It is well known that natural convection flows in a differentially heated cavity without a fin are determined by three governing dimensionless parameters (Bachelor 1954): the Rayleigh number (Ra), the Prandtl number (Pr) and the aspect ratio (A), defined respectively as follows:

$$Ra = \frac{g\beta\Delta T H^3}{\nu\kappa}, \quad Pr = \frac{\nu}{\kappa}, \quad A = \frac{H}{L}. \tag{5}$$

For the present case with a fin on the sidewall, the fin length is also a governing parameter, which will be confirmed in the following section. Furthermore, a Rayleigh number (Ra_h) is also adopted, which is defined in terms of the half-height of the heated wall ($h = H/2$) as follows:

$$Ra_h = \frac{g\beta\Delta T h^3}{\nu\kappa}. \tag{6}$$

It is worth noting that the dynamic mechanisms and scaling relations of the transient thermal boundary layer flow in a differentially heated cavity are different between the cases with $Pr > 1$ and $Pr < 1$ (see e.g. Patterson & Imberger 1980; Lin & Armfield 2005). In the subsequent scaling analysis and numerical simulations, only working fluids with $Pr > 1$ are considered.

For the purpose of illustrating the transient natural convection flows around the fin, a typical numerically calculated flow development as depicted by isotherms is presented in figure 2, in which $Ra_h = 2.29 \times 10^8$, $Pr = 100$, and the time has been non-dimensionalized by $h^2/(\kappa Ra_h^{1/2})$. Clearly, an important feature of the transient natural convection flows in the presence of the fin is the formation and evolution of two intrusions: one underneath the ceiling and the other underneath the fin, as seen in figure 2(a). The intrusions and the vertical thermal boundary layers upstream and downstream of the fin are identical at the very early stage (also refer to the experimental visualizations of Xu *et al.* 2008). However, the similarity between the flows upstream and downstream of the fin disappears after the lower intrusion front bypasses the fin, as shown in figure 2(b). At this time, a starting plume has formed, and the head of the plume rises towards the ceiling. With the passage of time, the plume front ascends until it strikes and is entrained into the intrusion under the ceiling (Xu *et al.* 2008). The subsequent plume flow is drawn towards the vertical thermal boundary layer downstream of the fin, as shown in figure 2(c). Indeed, the thermal flow above the fin becomes increasingly closer to the fin as time increases further; that is, a horizontal fluid layer above the fin eventually forms (figure 2d). In what follows, a scaling analysis is carried out based on the governing equations (1)–(4) in order to quantify the transient flows around the fin until the stage depicted in figure 2(d).

2.1. *Vertical thermal boundary layer with a fin*

In this section, following the arguments for the case without a fin by Patterson & Imberger (1980) and Lin *et al.* (2009), we will obtain the major scaling relations of the thermal boundary layer upstream of the fin with a brief discussion of possible dynamics or energy balances.
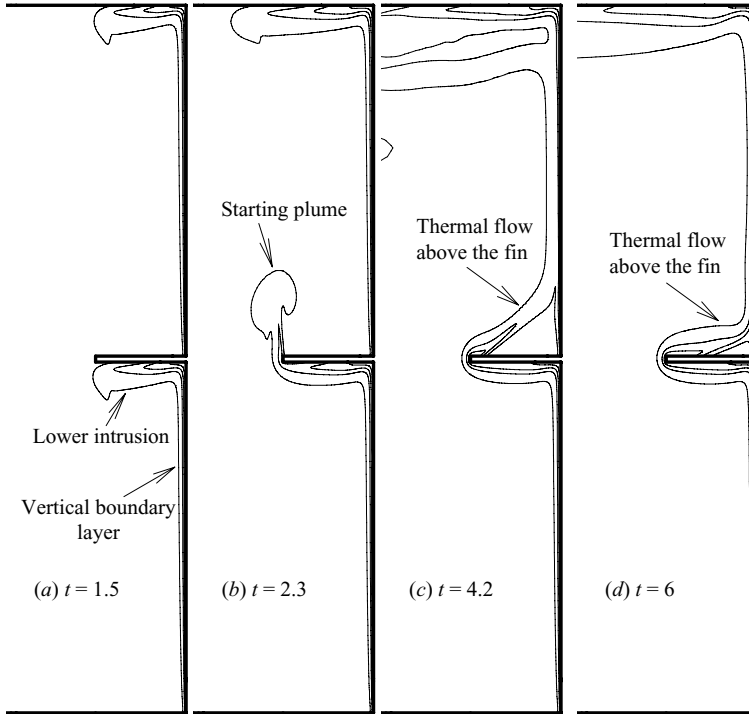
FIGURE 2. Typical transient natural convection flows around the fin at different times for $Ra_h = 2.29 \times 10^8$ and $Pr = 100$ (isotherms with a contour interval of 0.25).

Following sudden heating, heat conduction through the sidewall results in a growing thermal boundary layer adjacent to the finned sidewall, which is separated into two sections by the fin (figure 2a). For both sections, the order of the unsteady term in the energy equation (4) is $O(\Delta T/t)$; the order of the advection term is $O(v_T \Delta T/h)$; and the order of the conduction term is $O(\kappa \Delta T/\delta_T^2)$, where δ_T and v_T are the thickness and velocity scales of the thermal boundary layer (figure 3). Therefore, the ratio of the advection term to the unsteady term is $O(v_T t/h)$. Note that since the temperature of the fluid entrained into the upstream thermal boundary layer is T_0 (the initial temperature of the interior fluid) and that discharged out from the thermal boundary layer is $T_0 + \Delta T$ (the same as the temperature of the sidewall), the temperature difference scale of the thermal boundary layer is ΔT. For a sufficiently small time t, $v_T t < h$ and thus the advection term is insignificant compared with the unsteady term. The initial energy balance is therefore between the conduction term and the unsteady term, which yields a thickness scale of the thermal boundary layer (see Patterson & Imberger 1980)

$$\delta_T \sim (\kappa t)^{1/2}. \tag{7}$$

For the vertical thermal boundary layer on either side of the fin, the order of the unsteady term in (3) is $O(v_T/t)$; the order of the advection term is $O(v_T^2/h)$; the order of the viscous term is $O(\nu v_T/\delta_T^2)$; and the buoyancy term is $O(g\beta \Delta T)$. The ratio of the advection term to the unsteady term of (3) is $O(v_T t/h)$. Similar to the above argument for the initial energy balance, for a sufficiently small time the advection term of (3) is also insignificant compared with the unsteady term because $v_T t < h$. Furthermore, since the ratio of the viscous term to the unsteady term is $O(\nu t/\delta_T^2) \sim Pr$, for $Pr > 1$
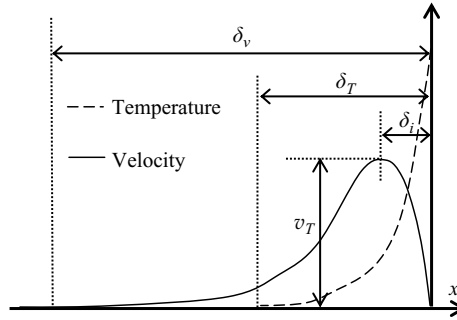
FIGURE 3. Schematic of the temperature and velocity profiles of a fluid boundary layer adjacent to a vertical thermal wall.

the unsteady term is also insignificant compared with the viscous term. Therefore, within a sufficiently small time for $Pr > 1$, both the unsteady and advection terms of (3) are negligibly small in comparison with the other terms, and the balance is between the viscous term and the buoyancy term.

The fluid boundary layer adjacent to a vertical thermal wall includes three sub-layers (see Lin *et al.* 2009): an inner viscous layer (δ_i), a viscous layer (δ_v) and the above-mentioned thermal layer (δ_T), which are illustrated in figure 3. The balance between the viscous term and the buoyancy term for a sufficiently small time yields a velocity scale for the inner viscous layer (see Lin *et al.* 2009):

$$v_T \sim \frac{g\beta\Delta T}{\nu}\delta_i^2. \tag{8}$$

For the fluid layer within the thermal boundary layer but outside the inner viscous layer, the balance of (3) is still between the buoyancy term and the viscous term, which may be integrated and expressed as

$$0 \sim \nu\left(\frac{\partial v}{\partial x}\right)_{\delta_i}^{\delta_T} + g\beta\int_{\delta_i}^{\delta_T} T\,dx. \tag{9}$$

The argument of Lin *et al.* (2009) suggested that $(\partial v/\partial x)_{\delta_i} = 0$ since the maximum velocity appears at $x = \delta_i$, $(\partial v/\partial x)_{\delta_T} \sim v_T/(\delta_v - \delta_i)$, and $g\beta\int_{\delta_i}^{\delta_T} T\,dx \sim g\beta\Delta T(\delta_T - \delta_i)$. Therefore, we may obtain a velocity scale as follows:

$$v_T \sim \frac{g\beta\Delta T}{\nu}(\delta_T - \delta_i)(\delta_v - \delta_i). \tag{10}$$

Considering (7), (8) and (10) as well as the thickness of the viscous boundary layer $\delta_v \sim (\nu t)^{1/2}$ (see Patterson & Imberger 1980), a thickness scale and an unsteady velocity scale for the inner viscous layer may be obtained as follows:

$$\delta_i \sim \frac{\delta_T}{1 + Pr^{-1/2}}, \tag{11a}$$

$$v_T \sim \frac{\kappa^2 Ra_h}{h^3\left(1 + Pr^{-1/2}\right)^2}t. \tag{11b}$$

The scaling relation (11a) shows that the thickness of the thermal boundary layer approaches that of the inner viscous layer as the Prandtl number increases. The scaling relation (10) is not applicable for $Pr \to \infty$ because in this case the assumption of three sub-layers does not hold.

It is clear that with the passage of time, the velocity increases, as specified by (11*b*). As a result, more heat is convected away and thus the advection term of the energy equation (4) becomes increasingly significant until the heat convected away ultimately balances the heat conducted from the sidewall. Using (7) and (11*b*), the balance between the advection term and the conduction term in (4) results in a time scale (t_s):

$$t_s \sim \frac{h^2 \left(1 + Pr^{-1/2}\right)}{\kappa \, Ra_h^{1/2}}, \tag{12}$$

after which the thermal boundary layer enters a steady state. Substituting (12) into (7) and (11*b*), we obtain the thickness and velocity scales of the thermal boundary layer on either side of the fin at the boundary layer steady state

$$\delta_{Ts} \sim \frac{h \left(1 + Pr^{-1/2}\right)^{1/2}}{Ra_h^{1/4}}, \tag{13a}$$

$$v_{Ts} \sim \frac{\kappa \, Ra_h^{1/2}}{h \left(1 + Pr^{-1/2}\right)}. \tag{13b}$$

2.2. *Lower intrusion under the fin*

Figure 2(*a*) shows that due to the presence of the fin, a lower intrusion, a typical horizontal gravity flow, forms underneath the fin. A corresponding intrusion forms under the ceiling of the cavity. Scaling analyses of horizontal gravity flows have been performed by Patterson & Imberger (1980) and Didden & Maxworthy (1982), in which the flow rate Q to the intrusion is assumed to be constant. Huppert (1982) and Maxworthy (1983) investigated a horizontal gravity flow with an unsteady flow rate in which the total volume of buoyant fluid in the horizontal gravity flow increases with time according to t^α (where α is a constant). In the present case, the lower intrusion is more complex than those considered in the previous studies. This is because the thickness and velocity of the thermal boundary layer upstream of the fin (which discharges into the horizontal lower intrusion) and upstream of the ceiling (which discharges into the horizontal intrusion beneath the ceiling) initially increase with time and then approach a constant value, as specified in (7) and (11)–(13). Consequently, neglecting entrainment, the volumetric flow rate to the intrusion may be expressed as

$$Q \sim u_I \delta_I \sim v_T \delta_T \sim \begin{cases} \dfrac{\kappa^{5/2} Ra_h}{h^3 \left(1 + Pr^{-1/2}\right)^2} t^{3/2}, & t < t_s, \\[3mm] \dfrac{\kappa \, Ra_h^{1/4}}{\left(1 + Pr^{-1/2}\right)^{1/2}}, & t > t_s, \end{cases} \tag{14}$$

where u_I and δ_I denote the velocity and the thickness of the two intrusions, respectively.

The results of Huppert (1982) and Maxworthy (1983) show that, for a two-dimensional intrusion, if $\alpha > 7/4$ the intrusion is initially governed by a buoyancy-viscosity balance, then by a buoyancy-inertia balance. For the present case, the time power of the flow rate (14) is $3/2$ for $t < t_s$, and therefore the time power of the total volume of the lower intrusion ($\sim Qt$) is $\alpha = 5/2 (> 7/4)$, and thus the buoyancy-viscous balance initially applies. The transition from the buoyancy-viscous to buoyancy-inertial flow regimes occurs at a time scale t_v (at which the ratio of the

viscous to inertial term is unity and the two terms are comparable) given by (also see Huppert 1982)

$$t_v \sim \frac{h^2 Pr^{5/3}\left(1 + Pr^{-1/2}\right)^{8/3}}{\kappa Ra_h^{2/3}}. \tag{15}$$

The above description of the intrusion applies so long as the flow rate to the intrusion increases with time until $t \sim t_s$, where t_s is given by (12). Thus, if $t_v < t_s$, the intrusion will be initially governed by a buoyancy-viscous balance, followed by a buoyancy-inertial balance. For the buoyancy-viscous flow regime, by following the argument of Huppert (1982) or directly by considering (14) and the balance between the buoyancy-induced horizontal pressure gradient ($g\beta\Delta T\delta_I / u_I t$; also see Patterson & Imberger 1980) and the viscous term ($\nu u_I/\delta_I^2$) in (2), the thickness and velocity scales of the lower intrusion may be obtained as

$$\delta_{Iv} \sim \left(\frac{\nu t Q^2}{g\beta\Delta T}\right)^{1/5} \sim \frac{\kappa^{4/5} Ra_h^{1/5} t^{4/5}}{h^{3/5}\left(1 + Pr^{-1/2}\right)^{4/5}}, \tag{16a}$$

$$u_{Iv} \sim \frac{Q}{\delta_{Iv}} \sim \frac{\kappa^{17/10} Ra_h^{4/5} t^{7/10}}{h^{12/5}\left(1 + Pr^{-1/2}\right)^{6/5}}. \tag{16b}$$

Furthermore, once the transition to the buoyancy-inertial flow regime occurs, the thickness and velocity scales under the balance between the buoyancy-induced horizontal pressure gradient ($g\beta\Delta T\delta_I / (u_I t)$) and the inertial term (u_I/t) may be expressed as

$$\delta_{Ig} \sim \frac{\kappa Ra_h^{1/3} t}{h Pr^{1/3}\left(1 + Pr^{-1/2}\right)^{4/3}}, \tag{17a}$$

$$u_{Ig} \sim \frac{\kappa^{3/2} Pr^{1/3} Ra_h^{2/3} t^{1/2}}{h^2\left(1 + Pr^{-1/2}\right)^{2/3}}. \tag{17b}$$

The transition from the buoyancy-viscous flow regime to the buoyancy-inertial flow regime occurs only if $t_v < t_s$. A comparison of these two time scales (t_v and t_s) shows that for $Ra_h > Pr^{10}(1 + Pr^{-1/2})^{10}$, then $t_v < t_s$; otherwise $t_s < t_v$. Accordingly, the scaling analysis of the lower intrusion in what follows is described for the two cases of $Ra_h > Pr^{10}(1 + Pr^{-1/2})^{10}$ and $Ra_h < Pr^{10}(1 + Pr^{-1/2})^{10}$, respectively.

For the case of $Ra_h > Pr^{10}(1 + Pr^{-1/2})^{10}$, when $t < t_s$, the development of the lower intrusion with an unsteady flow rate is described by (15)–(17). When $t > t_s$, the flow rate to the lower intrusion is constant given by (14). Accordingly, substituting (12) into (17a) and (17b), the steady thickness and velocity scales may be expressed as

$$\delta_{Igs} \sim \frac{h}{Pr^{1/3}\left(1 + Pr^{-1/2}\right)^{1/3} Ra_h^{1/6}}, \tag{18a}$$

$$u_{Igs} \sim \frac{\kappa Pr^{1/3} Ra_h^{5/12}}{h\left(1 + Pr^{-1/2}\right)^{1/6}}. \tag{18b}$$

With the passage of time, the viscous term of the lower intrusion with a steady flow rate becomes increasingly important, until the time at which the viscous and inertial terms balance, yielding a time scale

$$t_g \sim \frac{h^2}{\kappa Pr^{5/3}\left(1 + Pr^{-1/2}\right)^{2/3} Ra_h^{1/3}}. \tag{19}$$

If $t \gg t_g$, the balance is between the buoyancy-induced horizontal pressure gradient and the viscous term in (2) again, yielding a thickness scale and a velocity scale

$$\delta_{Ivs} \sim \frac{\kappa^{1/5} h^{3/5}}{\left(1 + Pr^{-1/2}\right)^{1/5} Ra_h^{1/10}} t^{1/5}, \tag{20a}$$

$$u_{Ivs} \sim \frac{\kappa^{4/5} Ra_h^{7/20}}{h^{3/5} \left(1 + Pr^{-1/2}\right)^{3/10}} t^{-1/5}. \tag{20b}$$

The scale (20b) indicates that the velocity of the lower intrusion at this stage reduces with time although the balance is still between the buoyancy-induced horizontal pressure gradient and viscous terms.

For the purpose of illustrating the evolution of the flow regimes with time, figure 4(a) presents a schematic of the dependence of the velocity on time under different flow regimes for a typical case of $Ra_h > Pr^{10}(1 + Pr^{-1/2})^{10}$ in which the velocity is calculated using (16b), (17b), (18b) and (20b) respectively. Note that the velocity and the time in figure 4 have been non-dimensionalized by $(\kappa Ra_h^{1/2})/h$ and $h^2/(\kappa Ra_h^{1/2})$, respectively.

For the case of $Ra_h < Pr^{10}(1 + Pr^{-1/2})^{10}$, since $t_s < t_v$, the transition from the buoyancy-viscous flow regime to the buoyancy-inertial flow regime does not occur. For $t > t_s$, the flow is still governed by a buoyancy-viscous balance. The buoyancy-viscous flow regimes for the case of $Ra_h < Pr^{10}(1 + Pr^{-1/2})^{10}$ are illustrated in figure 4(b).

It is worth noting that for the case of $Ra_h < Pr^{10}(1 + Pr^{-1/2})^{10}$, there does not exist a buoyancy-inertial flow regime. Therefore, $Ra_h \sim Pr^{10}(1 + Pr^{-1/2})^{10}$ may be regarded as a critical value determining whether the transition to the buoyancy-inertial flow regime would occur, as seen in figure 4(c). That is, the buoyancy-inertial flow regime occurs only on the left side of the curve of $Ra_h = Pr^{10}(1 + Pr^{-1/2})^{10}$ in the $Ra_h - Pr$ plane.

The scaling relations (12), (15) and (19) specify the times at which transitions of the flow regimes occur. According to these time scales, we may further predict the distances over which each flow regime applies and thus identifies the possible flow regimes of the lower intrusion for different fin lengths.

For $Ra_h > Pr^{10}(1 + Pr^{-1/2})^{10}$, since $t_v < t_s$, considering the velocity scale (16b) within the time scale t_v, we obtain the distance (l_v) over which the buoyancy-viscous flow regime applies as

$$l_v \sim u_{Iv} t \left|_{t \sim t_v} \right. \sim \frac{h Pr^{17/6} \left(1 + Pr^{-1/2}\right)^{10/3}}{Ra_h^{1/3}}. \tag{21}$$

The total distance (l_{gs}) through which the lower intrusion front with an unsteady flow rate penetrates may be estimated by

$$l_{gs} \sim u_{Igs} t \left|_{t \sim t_s} \right. \sim \frac{h Pr^{1/3} \left(1 + Pr^{-1/2}\right)^{5/6}}{Ra_h^{1/12}}. \tag{22}$$

Furthermore, the distance (l_{gsg}) at which the transition from the buoyancy-inertial flow regime to the buoyancy-viscous flow regime with a steady flow rate occurs may be given by

$$l_{gsg} \sim u_{Igs} t \left|_{t \sim t_g} \right. \sim \frac{h Ra_h^{1/12}}{Pr^{4/3} \left(1 + Pr^{-1/2}\right)^{5/6}}. \tag{23}$$
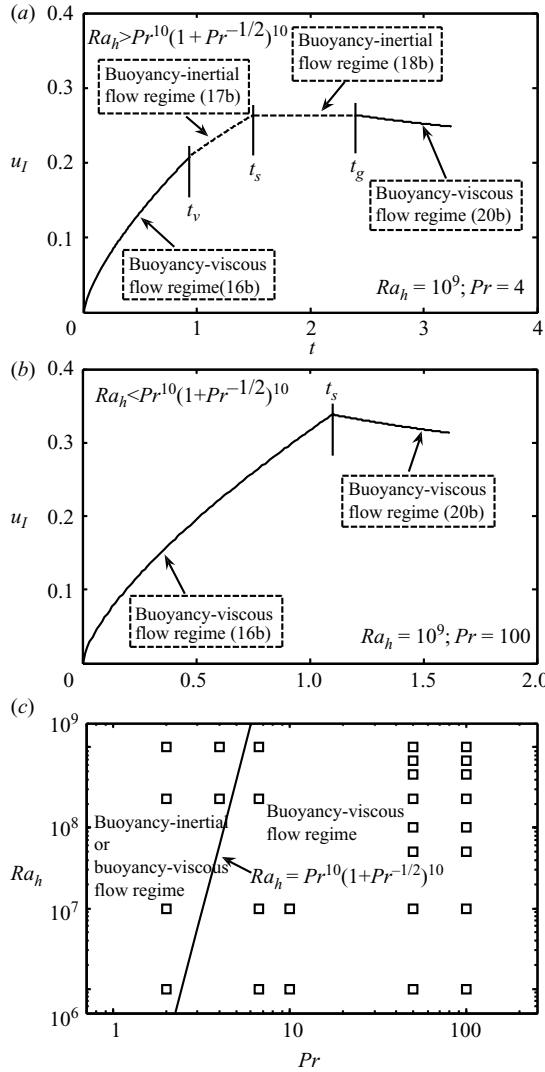
FIGURE 4. Possible buoyancy-inertial and buoyancy-viscous intrusion flow regimes. (*a*) Velocity against time for the case of $Ra_h = 10^9$ and $Pr = 4$. (*b*) Velocity against time for the case of $Ra_h = 10^9$ and $Pr = 100$. (*c*) Possible buoyancy-inertial and buoyancy-viscous intrusion flow regimes for different Rayleigh and Prandtl numbers (the squares show the Rayleigh and Prandtl numbers of direct numerical simulations in this paper).

In summary, for different fin lengths in the case of $Ra_h > Pr^{10}(1 + Pr^{-1/2})^{10}$, the flow regimes of the lower intrusion may be described in terms of the fin length as follows:

(i) $l < l_v$. The lower intrusion front underneath the fin travels under a buoyancy-viscous balance with an unsteady flow rate.

(ii) $l_v < l < l_{gs}$. The lower intrusion front initially travels under the buoyancy-viscous balance and then under the buoyancy-inertial balance, and the flow rate is unsteady until the lower intrusion bypasses the fin.

(iii) $l_{gs} < l < l_{gsg}$. The transition of the lower intrusion from the buoyancy-viscous flow regime to the buoyancy-inertial flow regime occurs similar to the case of $l_v < l < l_{gs}$, but the flow rate is steady when the lower intrusion bypasses the fin.

(iv) $l > l_{gsg}$. The transitions of the lower intrusion from the buoyancy-viscous flow regime to the buoyancy-inertial flow regime with an unsteady flow rate and then from the buoyancy-inertial flow regime to the buoyancy-viscous flow regime with a steady flow rate are expected. When the lower intrusion bypasses the fin, the flow rate is steady.

For the case of $Ra_h < Pr^{10}(1 + Pr^{-1/2})^{10}$, since $t_s < t_v$, the lower intrusion front travels under a buoyancy-viscous balance with an unsteady flow rate. Using (16*b*), the distance through which the lower intrusion front with an unsteady flow rate penetrates may be expressed as

$$l_{vs} \sim u_{Iv} t \,|_{t \sim t_s} \sim \frac{h\left(1 + Pr^{-1/2}\right)^{1/2}}{Ra_h^{1/20}}. \tag{24}$$

Therefore, for $l < l_{vs}$, the lower intrusion travels under the buoyancy-viscous balance, and the flow rate is unsteady when the lower intrusion bypasses the fin. For $l < l_{vs}$, the lower intrusion first travels under the buoyancy-viscous balance with an unsteady flow rate, and then the flow rate becomes steady when the lower intrusion travels beyond l_{vs}.

2.3. *Starting plume originating from the lower intrusion*

When the lower intrusion bypasses the fin, it may be considered as a horizontal jet with an initial horizontal velocity. If the exiting horizontal velocity is low (which was confirmed by the numerical and experimental results of Xu *et al.* 2008, 2009), the exiting lower intrusion quickly ascends due to buoyancy effects and a starting plume forms, as illustrated in figure 2(*b*). Studies of starting plumes have been extensively reported (see e.g. Turner 1962; Shlien 1976; List 1982; Campbell, Griffiths & Hill 1989; Moses, Zocchi & Libchaber 1993; Kaminski & Jaupart 2003). Most of the previous studies focused on a starting plume generated by a point or a line heating source, and the starting plume with a steady flow rate has been given much attention (see Kaminski & Jaupart 2003). In this section, we will consider a starting plume originating from the lower intrusion bypassing the fin (a horizontal jet), possibly with either a steady or unsteady flow rate.

The flow rate to the starting plume here is unsteady if the fin length is sufficiently small, (i.e. $l < l_{gs}$ or l_{vs}, see (22) and (24)). Accordingly, we assume that, in general, the flow rate to the plume varies with time and has a power-law function of time as follows:

$$Q \sim v_P \delta_P \sim q_c t^{\gamma}, \tag{25}$$

where v_P and δ_P are the velocity and the thickness of the starting plume, q_c is a coefficient, t is the time measured from the formation of the starting plume and γ is a non-negative constant.

The horizontal component of the plume velocity is small compared with the vertical velocity component (also see Xu *et al.* 2008, 2009). Therefore, we consider only the vertical momentum equation (3). In the starting plume, the order of the inertial term of (3) is $O(v_P/t)$, the order of the viscous term $O(\nu v_P/\delta_P^2)$ and the buoyancy term $O(g\beta\Delta T)$. Using (25), the balance between the viscous term and the buoyancy

term in (3) yields the thickness and velocity scales of the starting plume

$$\delta_{Pv} \sim \left(\frac{\nu Q}{g\beta\Delta T} \right)^{1/3} \sim \left(\frac{\nu q_c t^{\gamma}}{g\beta\Delta T} \right)^{1/3}, \qquad (26a)$$

$$v_{Pv} \sim \frac{g\beta\Delta T}{\nu} \left(\frac{\nu Q}{g\beta\Delta T} \right)^{2/3} \sim \left(\frac{g\beta\Delta T}{\nu} \right)^{1/3} q_c^{2/3} t^{2\gamma/3}. \qquad (26b)$$

On the other hand, the balance between the inertial term and the buoyancy term in (3) yields the thickness and velocity scales under the buoyancy-inertial balance:

$$\delta_{Pg} \sim \frac{q_c t^{\gamma-1}}{g\beta\Delta T}. \qquad (27a)$$

$$v_{Pg} \sim g\beta\Delta T t, \qquad (27b)$$

Based on (26a) and (27a), the ratio of the inertial term to the viscous term may be expressed as

$$\frac{\delta_{Pv}^2}{\nu t} \sim \left(\frac{q_c^2 t^{2\gamma-3}}{\nu(g\beta\Delta T)^2} \right)^{1/3}, \qquad (28a)$$

$$\frac{\delta_{Pg}^2}{\nu t} \sim \frac{q_c^2 t^{2\gamma-3}}{\nu(g\beta\Delta T)^2}. \qquad (28b)$$

If the ratio of the inertial term to the viscous term is of the order of unity, for either (28a) or (28b), we obtain a time scale

$$t_{Pv} \sim \left(\frac{\nu^{1/2} g\beta\Delta T}{q_c} \right)^{1/(\gamma-3/2)}, \qquad (29)$$

where t_{Pv} is a time scale at which the viscous and inertial terms are of equal significance.

Clearly, for $\gamma > \gamma_c = 3/2$, if $t \ll t_{Pv}$, the ratio of the inertial term to the viscous term (either (28a) or (28b)) is much smaller than unity; that is, the buoyancy-viscous flow regime initially dominates the starting plume with the thickness and velocity scales specified by (26a) and (26b). If $t \gg t_{Pv}$, the ratio of the inertial term to the viscous term is much larger than unity and the buoyancy-inertial flow regime applies to the starting plume with the thickness and velocity scales specified by (27a) and (27b). On the other hand, for $\gamma < \gamma_c$, if $t \ll t_{Pv}$, the ratio of the inertial term to the viscous term (either (28a) or (28b)) is much larger than unity, and thus the starting plume under a buoyancy-inertial balance initially ascends with the thickness and velocity scales given by (27a) and (27b). However, if $t \gg t_{Pv}$, the ratio of the inertial term to the viscous term is much smaller than unity and the starting plume is dominated by a buoyancy-viscous balance with the thickness and the velocity specified by (26a) and (26b), respectively.

It is interesting to note that, for the case of $\gamma = \gamma_c$, the dynamic balance is independent of time (see (28a) and (28b)); that is, if $q_c \ll \nu^{1/2} g\beta\Delta T$, the ratio of the inertial term to the viscous term is much less than unity and, thus, the balance is always between the buoyancy term and the viscous term. On the other hand, if $q_c \gg \nu^{1/2} g\beta\Delta T$, a buoyancy-inertial balance always dominates the starting plume. For $q_c \sim \nu^{1/2} g\beta\Delta T$, the inertial and viscous terms are comparable.

For the starting plume bypassing the fin, we first consider a simple case of $l > l_{gs}$ or l_{vs}; that is, the flow rate to the starting plume is constant,

$Q \sim q_c \sim \kappa Ra_h^{1/4}/(1 + Pr^{-1/2})^{1/2}$ (also see (14)) and $\gamma = 0$. Substituting q_c and γ into (29), a time scale is given by

$$t_{Pv} \sim \frac{h^2}{\kappa Pr \left(1 + Pr^{-1/2}\right)^{1/3} Ra_h^{1/2}}. \tag{30}$$

As previously discussed, for the case of $\gamma(=0) < \gamma_c$, the balance is mainly between the buoyancy term and the inertial term if $t \ll t_{Pv}$. Hence, recognizing $q_c \sim \kappa Ra_h^{1/4}/(1 + Pr^{-1/2})^{1/2}$, $\gamma = 0$ in (27a) and (27b), the thickness and velocity scales of the starting plume are obtained as follows:

$$\delta_{Pg} \sim \frac{h^3}{\kappa Pr \left(1 + Pr^{-1/2}\right)^{1/2} Ra_h^{3/4} t}, \tag{31a}$$

$$v_{Pg} \sim \frac{\kappa^2 Pr Ra_h t}{h^3}. \tag{31b}$$

When $t \gg t_{Pv}$, the buoyancy term balances the viscous term in (3), as previously discussed. Substituting $q_c \sim \kappa Ra_h^{1/4}/(1 + Pr^{-1/2})^{1/2}$ and $\gamma = 0$ into (26a) and (26b), we obtain the steady thickness and velocity scales

$$\delta_{Pv} \sim \frac{h}{\left(1 + Pr^{-1/2}\right)^{1/6} Ra_h^{1/4}}, \tag{32a}$$

$$v_{Pv} \sim \frac{\kappa Ra_h^{1/2}}{h \left(1 + Pr^{-1/2}\right)^{1/3}}. \tag{32b}$$

We may also consider a starting plume bypassing the fin with an unsteady flow rate ($l < l_{gs}$ or l_{vs}). When $t < t_s$, according to the scaling relation (14), the time power of the unsteady flow rate is $3/2$ and $q_c \sim \kappa^{5/2} Ra_h/(h^3(1 + Pr^{-1/2})^2) < \nu^{1/2} g\beta \Delta T$ (note that $Pr > 1$ in this study); that is, the balance is between the viscous term and the buoyancy term. Therefore, considering $Q \sim \kappa^{5/2} Ra_h t^{3/2}/(h^3(1 + Pr^{-1/2})^2)$, this balance yields the thickness and velocity scales under the buoyancy-viscous balance

$$\delta_{Pv} \sim \frac{\kappa^{1/2} t^{1/2}}{(1 + Pr^{-1/2})^{2/3}}, \tag{33a}$$

$$v_{Pv} \sim \frac{\kappa^2 Ra_h t}{h^3(1 + Pr^{-1/2})^{4/3}}. \tag{33b}$$

Note that since t here is measured from the initiation of sudden heating in the flow rate calculation $Q \sim \kappa^{5/2} Ra_h t^{3/2}/(h^3(1 + Pr^{-1/2})^2)$, t in (33a) and (33b) also needs to be measured from the initiation of sudden heating.

When the flow rate is steady, we may obtain the same velocity and thickness scales as (31)–(32). That is, the balance is between the inertial term and the buoyancy term for $t \ll t_{Pv}$ and the starting plume ascends with the thickness and the velocity given by (31a) and (31b); and the starting plume is dominated by a buoyancy-viscous balance for $t \gg t_{Pv}$ and has a steady velocity and thickness specified by (32a) and (32b).

2.4. Horizontal thermal flow above the fin

In the early stage, since the thermal flow above the fin is complex and has both horizontal and vertical components of the velocity (see figure 2c), a detailed scaling analysis of the horizontal thermal flow above the fin is not possible. Here, we consider only the case with a fully developed thermal flow above the fin; that is, the thermal flow above the fin is approximately horizontal (figure 2d) and has a steady flow rate

expressed by (see (14))

$$Q \sim u_A \delta_A \sim \frac{\kappa Ra_h^{1/4}}{\left(1 + Pr^{-1/2}\right)^{1/2}}, \tag{34}$$

where u_A and δ_A are the velocity and thickness of the horizontal thermal flow above the fin, arising from the steady state of the thermal boundary layer upstream of the fin.

The horizontal thermal flow above the fin is driven by a buoyancy-induced horizontal pressure gradient. In the horizontal thermal layer above the fin, the order of the buoyancy-induced pressure is $O(\rho g \beta \Delta T \delta_A)$ (see Patterson & Imberger 1980). The length scale of the flow above the fin is l (the fin length), and the scale of the buoyancy-induced horizontal pressure gradient may be expressed by

$$\frac{1}{\rho} \frac{\partial p}{\partial x} \sim g \beta \Delta T \frac{\delta_A}{l}. \tag{35}$$

For the same flow, the order of the advection term in (2) is $O(u_A^2/l)$ and the order of the viscous term $O(\nu u_A/\delta_A^2)$. Using (34), the balance between the viscous term and the buoyancy-induced horizontal pressure gradient (35) yields the thickness and velocity scales of the thermal flow above the fin:

$$\delta_{Av} \sim \frac{l^{1/4} h^{3/4}}{\left(1 + Pr^{-1/2}\right)^{1/8} Ra_h^{3/16}}, \tag{36a}$$

$$u_{Av} \sim \frac{\kappa Ra_h^{7/16}}{l^{1/4} h^{3/4} \left(1 + Pr^{-1/2}\right)^{3/8}}. \tag{36b}$$

Furthermore, the balance between the advection term and the buoyancy-induced horizontal pressure gradient yields thickness and velocity scales under the buoyancy-advection balance

$$\delta_{Ag} \sim \frac{h}{Pr^{1/3} \left(1 + Pr^{-1/2}\right)^{1/3} Ra_h^{1/6}}, \tag{37a}$$

$$u_{Ag} \sim \frac{\kappa Pr^{1/3} Ra_h^{5/12}}{h \left(1 + Pr^{-1/2}\right)^{1/6}}. \tag{37b}$$

Based on (36a) and (36b) or (37a) and (37b), the ratio of the advection term to the viscous term $O(u_A \delta_A^2/(\nu l))$ may be expressed as

$$\frac{u_{Av} \delta_{Av}^2}{\nu l} \sim \left(\frac{h Ra_h^{1/12}}{l Pr^{4/3} \left(1 + Pr^{-1/2}\right)^{5/6}}\right)^{3/4}, \tag{38a}$$

$$\frac{u_{Ag} \delta_{Ag}^2}{\nu l} \sim \frac{h Ra_h^{1/12}}{l Pr^{4/3} \left(1 + Pr^{-1/2}\right)^{5/6}}. \tag{38b}$$

Assuming that the ratio of the advection term to the viscous term is unity, for either (38a) or (38b), we may obtain a critical fin length scale:

$$l_A \sim \frac{h Ra_h^{1/12}}{Pr^{4/3} \left(1 + Pr^{-1/2}\right)^{5/6}}. \tag{39}$$

Clearly, there is a transition from the buoyancy-inertial flow regime to the buoyancy-viscous flow regime at $l \sim l_A$. That is, if the fin is sufficiently short ($l \ll l_A$), the

ratio of the advection term to the viscous term is much larger than unity (refer to either (38*a*) or (38*b*)) and, thus, the thermal flow above the fin is governed by a buoyancy-advection balance with its velocity and thickness specified by (37*a*) and (37*b*). However, if the fin is sufficiently long ($l \gg l_A$), the ratio of the advection term to the viscous term is much smaller than unity and, thus, the thermal flow above the fin travels under a buoyancy-viscous balance with the thickness and the velocity given by (36*a*) and (36*b*), respectively.

3. Numerical procedures

For convenience, the variables in the governing equations are non-dimensionalized using the following scales: $x, y \sim h$; $t \sim h^2/(kRa_h^{1/2})$; $(T - T_0) \sim \Delta T$; $u, v \sim \kappa Ra_h^{1/2}/h$; and $\rho^{-1}\partial p/\partial x, \rho^{-1}\partial p/\partial y \sim \kappa^2 Ra_h/h^3$. Accordingly, a non-dimensional form of the governing equations is written as

$$\frac{\partial u}{\partial x} + \frac{\partial v}{\partial y} = 0, \tag{40}$$

$$\frac{\partial u}{\partial t} + u\frac{\partial u}{\partial x} + v\frac{\partial u}{\partial y} = -\frac{\partial p}{\partial x} + Pr\left(\frac{\partial^2 u}{\partial x^2} + \frac{\partial^2 u}{\partial y^2}\right), \tag{41}$$

$$\frac{\partial v}{\partial t} + u\frac{\partial v}{\partial x} + v\frac{\partial v}{\partial y} = -\frac{\partial p}{\partial y} + Pr\left(\frac{\partial^2 v}{\partial x^2} + \frac{\partial^2 v}{\partial y^2}\right) + PrRa_h T, \tag{42}$$

$$\frac{\partial T}{\partial t} + u\frac{\partial T}{\partial x} + v\frac{\partial T}{\partial y} = \frac{\partial^2 T}{\partial x^2} + \frac{\partial^2 T}{\partial y^2}. \tag{43}$$

All interior boundaries of the computational domain are assumed non-slip, and the fin and the top and bottom walls are assumed adiabatic, as indicated in §2. Initially, the working fluid is at rest and isothermal, and at $t = 0$ the temperature of the finned sidewall is raised to 1 and that of the opposite sidewall is lowered to -1.

The governing equations are implicitly solved using a finite-volume SIMPLE scheme. Second derivatives and linear first derivatives are approximated by a second-order centre-differencing scheme. The advection terms are discretized using a QUICK scheme (see Patterson & Armfield 1990). The time integration is by a second-order backward difference method. The discretized equations are iterated with specified under-relaxation factors.

Considering the special features of natural convection flows in a differentially heated cavity, a hybrid grid system is constructed with finer non-uniform grids concentrated in the proximity of all wall boundaries and a relatively coarse uniform grid in the interior region. In the wall boundary regions, the grid expands at a constant rate from the wall towards the interior edges of these regions. Similarly, the vicinity of the fin is finely meshed in order to accurately capture the features of the transient natural convection flows around the fin.

Grid dependence tests were conducted on a coarse grid of 163×333, a medium grid of 211×538 and a fine grid of 259×743, respectively. Note that since the computational domain around the fin is finely meshed in order to resolve the local flows around the fin, the resulting grids adopted here are much finer than what was recommended by Gelfgat (2007) for the flows in a cavity without a fin. Furthermore, in order to evaluate the effect of the three grid systems on the transient natural convection flows adjacent to the finned sidewall, a representative parameter is calculated from the numerical results: the volumetric flow rate of the vertical thermal boundary layer,
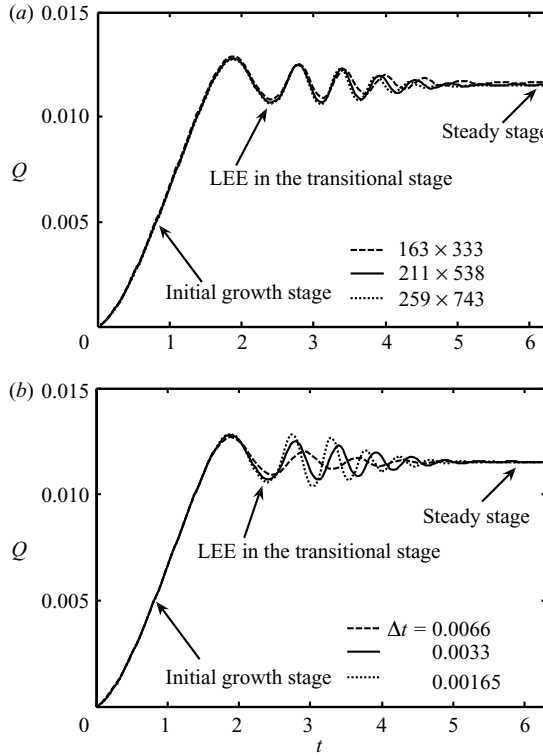
FIGURE 5. Time series of the calculated flow rate for $Ra_h = 10^9$ and $Pr = 6.63$ using different grid systems and time steps (where Δt is the time step).

which is given by (also see Lei & Patterson 2002)

$$Q = \int_{x_e}^{x_w} v \, dx, \qquad (44)$$

where Q is the non-dimensional volumetric flow across a horizontal sectional plane at the location of the maximum steady-state velocity in the vertical thermal boundary layer upstream of the fin; x_w and x_e are the x-coordinates of the sidewall and the interior edge of the vertical thermal boundary layer, which is defined as the location at which $T = 0.01$. The volumetric flow rate Q is non-dimensionalized using $\kappa Ra_h^{1/2}$.

Grid dependence tests were carried out for the case of the highest Rayleigh number ($Ra_h = 10^9$ and $Pr = 6.63$) in this study. Figure 5(a) shows time series of the volumetric flow rates calculated using the three grid systems. The numerical solutions with the two finer grid systems are consistent with a maximum variation of 2.8% in the transitional stage. Furthermore, the maximum variation between the flow rates calculated by the finest grid system and the coarsest grid system is 6.7%. Since this study is focused on the basic flows around the fin rather than the details of the LEE, either of the two finer grid systems may be used with a good accuracy in comparison with the coarsest grid system. In consideration of the computing time, the grid system of 211 (H) × 538 (L), with a grid inflation factor of 1.04 towards the centre of the domain in both the horizontal and vertical boundary zones, is adopted.

As indicated in figure 5(a), the development of the vertical thermal boundary layer includes an initial growth stage, a transitional stage and a steady stage (also see Xu

et al. 2008). In particular, in the transitional stage, the LEE of the vertical thermal boundary layer is clear (refer to Patterson *et al.* 2002 for more details about the LEE). Note that the steady stage here refers only to a state of the boundary layer adjacent to the finned sidewall, which occurs after the passage of the LEE and before the intrusion from the opposing sidewall strikes the finned sidewall. At this stage, the interior fluid remains isothermal. Previous studies (see e.g. Xu *et al.* 2009) show that after the intrusion from the opposing sidewall strikes the finned sidewall, the cavity flows eventually approach a steady state with a stratified interior fluid. Since different flow mechanisms are involved in the cavity flows with isothermal and stratified interior fluids, the latter steady state (for the cavity flows) is not considered in the present scaling analysis.

A time step dependence test was conducted with dimensionless time steps of 0.066, 0.033 and 0.0165, respectively, and the results are shown in figure 5(*b*). For the three cases with different time steps, there is no discernible difference in the calculated flow rates at the initial growth stage and the steady stage, but discernible variations can be seen in the transitional stage (LEE). This indicates that the basic flow is independent of the tested time steps except for the wave properties associated with the LEE. As mentioned above, this study focuses on the basic flow regimes of the natural convection flows around the fin rather than resolving the details of the LEE, the time step of 0.033 is adopted in consideration of the computing time and the numerical accuracy.

4. Numerical results and discussion

Based on the experimental model described by Xu *et al.* (2008), we adopted a fixed aspect ratio of the cavity ($A = 0.24$) in the present numerical simulations. Furthermore, the geometric dimensions of the fin are also fixed (here the fin length $l = h/3$ and the fin thickness $d = h/60$). Since unstable flows with strong oscillations are expected at very high Rayleigh numbers (refer to Janssen & Henkes 1995; Armfield & Janssen 1996; Janssen & Armfield 1996) but cannot be considered in the present scaling analysis, the Rayleigh numbers adopted in the present numerical simulations for the scaling validation are limited to $Ra_h = 10^9$. Moreover, cases with a wide range of Prandtl numbers from $Pr = 2$ to $Pr = 100$ are calculated here. The parameter values for the 32 numerical simulation runs presented in this paper are listed in table 1 and shown in figure 4(*c*).

4.1. *Demonstration of transient flow structures*

The lower intrusion is a representative transient flow structure of the natural convection flows around the fin. The scaling analysis in §2.2 indicates that for different parameter settings the lower intrusion could travel under different flow regimes. Figures 6(*a*) and 6(*b*) present isotherms and streamlines adjacent to the finned sidewall for a low Rayleigh number case with $Ra_h = 10^6$ and $Pr = 100$ (here $Ra_h < Pr^{10}(1 + Pr^{-1/2})^{10}$). The flow time is 1.1, the same order as t_s given by (12). Hence, the intrusion with a steady flow rate travels under the buoyancy-viscous flow regime. For the case presented in figures 6(*c*) and 6(*d*), in which $Ra_h = 10^9$ and $Pr = 2$ so that $Ra_h > Pr^{10}(1 + Pr^{-1/2})^{10}$, the flow time is 2.6, larger than t_s ($t_s \sim 1.7$ for this case) and smaller than t_g ($t_g \sim 7$ for this case), and the intrusion with a steady flow rate propagates under a buoyancy-inertial balance. Clearly, the intrusion with a steady flow rate under the buoyancy-viscous flow regime (figures 6*a* and 6*b*) is weaker compared with that under the buoyancy-inertial flow regime (figures 6*c* and 6*d*).

	Prandtl number (Pr)	Rayleigh number (Ra_h for cases with a fin and Ra for cases without a fin)	
		$Ra_h > Pr^{10}(1 + Pr^{-1/2})^{10}$	Ra_h or $Ra < Pr^{10}(1 + Pr^{-1/2})^{10}$
Fin	2	$10^9, 2.29 \times 10^8, 10^7, 10^6$	
	4	$10^9, 2.29 \times 10^8$	
	6.63		$10^9, 2.29 \times 10^8, 10^7, 10^6$
	10		$10^7, 10^6$
	50		$10^9, 6.87 \times 10^8, 4.58 \times 10^8,$ $2.29 \times 10^8, 10^8, 5 \times 10^7, 10^7, 10^6$
	100		$10^9, 6.87 \times 10^8, 4.58 \times 10^8,$ $2.29 \times 10^8, 10^8, 5 \times 10^7, 10^7, 10^6$
No fin	50		$10^9, 2.29 \times 10^8$
	100		$10^9, 2.29 \times 10^8$

TABLE 1. Parameters of numerical simulations.

(a) $t = 1.1$ (b) $t = 1.1$ (c) $t = 2.6$ (d) $t = 2.6$
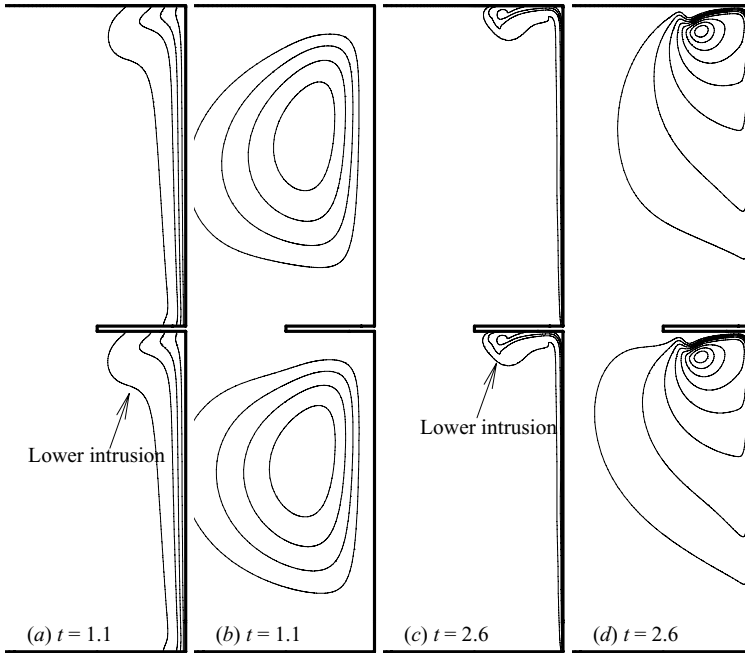
FIGURE 6. Intrusions under the buoyancy-viscous and the buoyancy-inertial flow regimes. (a) Isotherms with a contour interval of 0.25 and (b) streamlines with a contour interval of 0.013 for $Ra_h = 10^6$ and $Pr = 100$. (c) Isotherms with a contour interval of 0.25 and (d) streamlines with a contour interval of 0.0018 for $Ra_h = 10^9$ and $Pr = 2$.

The streamlines in figure 6(b) indicate that a circulation almost occupies the whole space at the upstream side of the lower intrusion. On the contrary, for $Ra_h = 10^9$ and $Pr = 2$, a head of the intrusion under the buoyancy-inertial flow regime may be clearly observed (figure 6c). The strong velocity shear in the intrusion head produces distinct circulations below the intrusion.
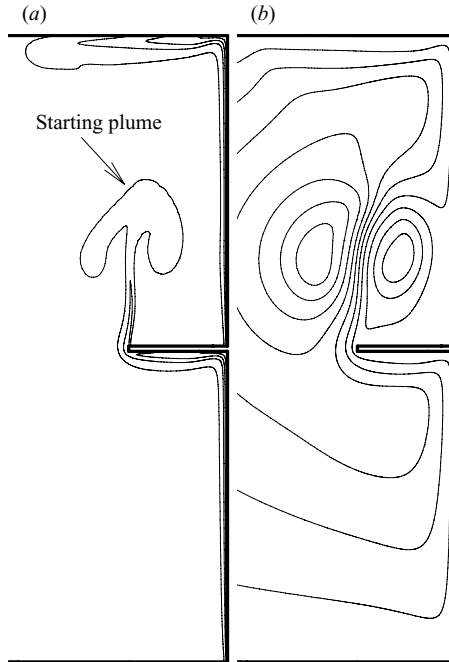
FIGURE 7. Starting plume under the buoyancy-viscous flow regime at $t = 2.8$. (*a*) Isotherms with a contour interval of 0.25 and (*b*) streamlines with a contour interval of 0.017 for $Ra_h = 2.29 \times 10^8$ and $Pr = 50$.

After the lower intrusion bypasses the fin, a starting plume is formed. Figure 7 shows a starting plume for $Ra_h = 2.29 \times 10^8$ and $Pr = 50$. Since $t = 2.8 > t_s \sim 1.1$ for this case, the flow rate to the plume is a constant value at this time. Furthermore, since the time for the lower intrusion to travel across the full length of the fin is 1.7, the time counted from the formation of the starting plume is $1.1 > t_{Pv} \sim 0.15$ (refer to (30)), and thus the buoyancy-viscous balance applies to the starting plume in figure 7. Clearly, due to entrainment by the downstream vertical thermal boundary layer, the temperature (figure 7a) and flow (figure 7b) structures of the starting plume are not symmetrical, which are different from those laminar starting plumes generated by a point or line heating source (refer to Campbell *et al.* 1989; Kaminski & Jaupart 2003).

Further numerical results show that the starting plume ascends until it strikes the intrusion under the ceiling. As time goes by, the thermal flow behind the plume front is drawn to the vertical thermal boundary layer downstream of the fin, as illustrated in figure 2(*c*). Figures 8(*a*) and 8(*b*) present the isotherms and streamlines for the case with a relatively low Rayleigh number ($Ra_h = 10^7$ and $Pr = 6.63$). The numerical results show that the thermal flow smoothly bypasses the fin, and the vertical thermal boundary layer downstream of the fin approaches a steady state after the early perturbations (the LEE and the lower intrusion).

Figures 8(*c*) and 8(*d*) present a representative case with a higher Rayleigh number $Ra_h = 2.29 \times 10^8$ (and $Pr = 6.63$). It is clear that the flow above the fin is unstable, which is illustrated by the intermittent plume entrained into the vertical thermal boundary layer in figures 8(*c*) and 8(*d*). The intermittent plume above the fin (figure 8c) in turn triggers oscillations of the downstream vertical thermal boundary layer,
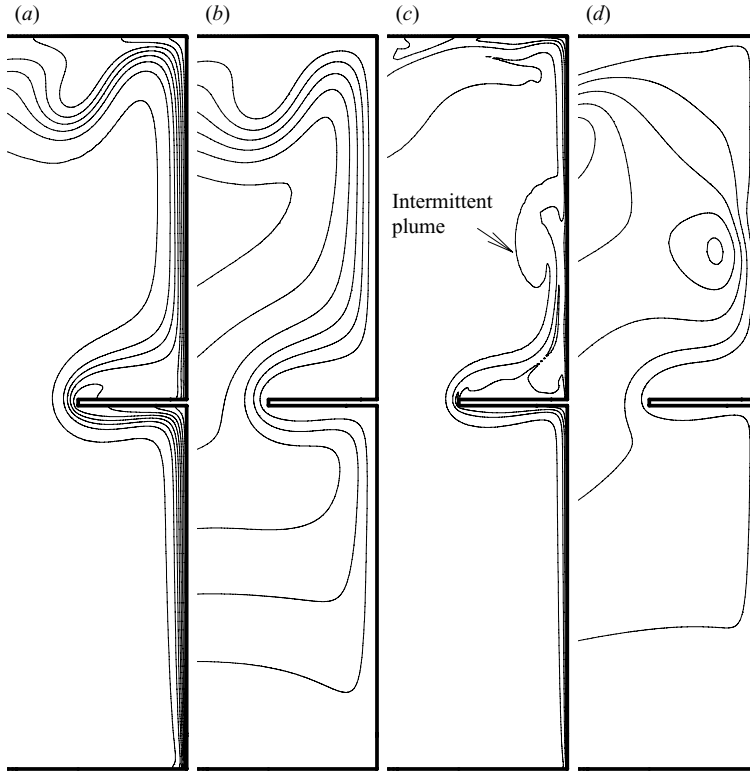
FIGURE 8. Natural convection flows around the fin under different flow regimes. (*a*) Isotherms with a contour interval of 0.125 and (*b*) streamlines with a contour interval of 0.0144 for $Ra_h = 10^7$ and $Pr = 6.67$ at $t = 6.3$. (*c*) Isotherms with a contour interval of 0.25 and (*d*) streamlines with a contour interval of 0.064 for $Ra_h = 2.29 \times 10^8$ and $Pr = 6.67$ at $t = 6.8$.

which was also confirmed by the corresponding experimental observations reported by Xu *et al.* (2008). As a consequence, the natural convection flows around the fin eventually approach a time-dependent periodic flow (refer to Xu *et al.* 2009 for details). Numerical simulations of Xu *et al.* (2009) showed that this instability originates from the unstable fluid layer with an adverse temperature gradient above the fin.

4.2. *Validations of selected scales*

In this section, the selected scales derived above, describing the transient natural convection flows around the fin, including the intrusion, the starting plume and the horizontal thermal flow above the fin, will be validated by the corresponding numerical results. The numerical results and validations of the vertical thermal boundary layer scales are described in detail by Lin *et al.* (2007, 2009), and thus are not repeated here. Note that for the convenience of validating the scaling relations obtained in § 2, dimensional time, velocity and thickness scales are adopted in this section. Furthermore, the fronts and edges of both the intrusions and the plume for the identification of the thicknesses and positions of these flows are assumed at a position where the temperature differs from the ambient by 1%.

4.2.1. *Intrusion*

The scaling relations show that the lower intrusion is initially time-dependent and governed by different dynamic balances. The scaling relations obtained in § 2.2 may
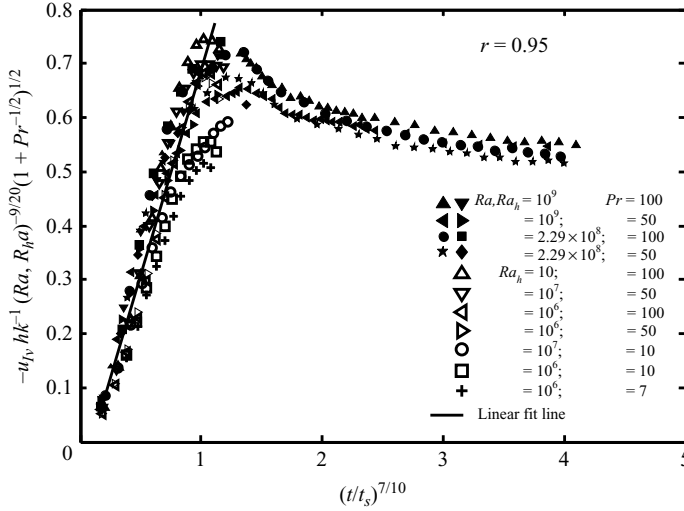
FIGURE 9. Dependence of the front velocity of the intrusion on time under the buoyancy-viscous flow regime with an unsteady flow rate for $Ra_h < Pr^{10}(1 + Pr^{-1/2})^{10}$.

be classified into four different flow regimes under which the lower intrusion travels: the buoyancy-viscous flow regime with an unsteady flow rate described by the stages of $t < t_v$ in figure 4(a) and $t < t_s$ in figure 4(b), the buoyancy-viscous flow regime with a steady flow rate by the stages of $t > t_g$ in figure 4(a) and $t > t_s$ in figure 4(b), the buoyancy-inertial flow regime with an unsteady flow rate by the stage of $t_v < t < t_s$ in figure 4(a), and the buoyancy-inertial flow regime with a steady flow rate by the stage of $t_s < t < t_g$ in figure 4(a). In this section, the calculated intrusion front velocity at various stages and the steady-state thickness of the intrusion are used to validate the corresponding scaling relations. Because the scaling is valid for both the intrusion under the fin and the intrusion under the ceiling, data from some cases with no fin are also presented here.

Consider first the case $Ra_h < Pr^{10}(1 + Pr^{-1/2})^{10}$. Here, the initial intrusion flow is governed by a buoyancy-viscous balance and, since $t_s < t_v$, the inflow to the intrusion from the vertical boundary layer becomes steady before a transition to a buoyancy-inertia balance occurs. The intrusion initially travels at a velocity specified by (16b). As noted above, because of the similarity between the lower intrusion under the fin and the intrusion under the ceiling of an un-finned cavity, we present two sets of numerical results for the cases with and without a fin in figure 9 in order to validate the scaling relation (16b); that is, the numerical results are obtained from the intrusion under the fin for the case with a fin and from the intrusion under the ceiling for the case without a fin. Note that the definitions of the Rayleigh numbers for the two sets of the numerical results are different (refer to (5) and (6)). Here, since the origin of the coordinate is at the centre of the cavity, the horizontal velocity of the lower intrusion front is negative.

In the velocity growth stage (that is, $t < t_s$), the front velocity (16b) may be written as $u_{Iv} \sim \kappa Ra_h^{9/20}(t/t_s)^{7/10}/(h(1 + Pr^{-1/2})^{1/2})$ and a corresponding form using Ra in place of Ra_h for the no-fin case. The normalized velocities $u_{Iv}hk^{-1}Ra_h^{-9/20}(1 + Pr^{-1/2})^{1/2}$ and $u_{Iv}hk^{-1}Ra^{-9/20}(1 + Pr^{-1/2})^{1/2}$ for the fin and no-fin cases, respectively, are plotted in figure 9 against $(t/t_s)^{7/10}$ over the numerically calculated range $Ra_h, Ra = 10^6 \sim 10^9$ and $Pr = 7 \sim 100$. For $t < t_s$, the relationship is close to linear, as shown in the figure,
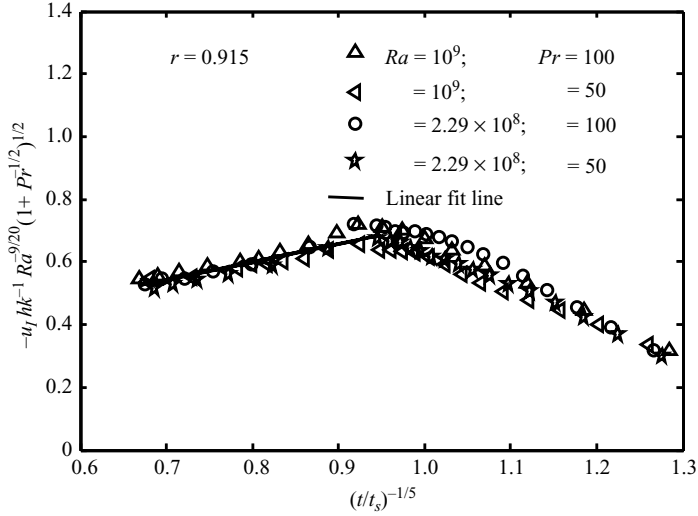
FIGURE 10. Dependence of the front velocity of the intrusion on time under the buoyancy-viscous flow regime with a steady flow rate for $Ra_h < Pr^{10}(1 + Pr^{-1/2})^{10}$.

with a correlation coefficient (r) of 0.95 over that range. The relatively large deviation close to $t \sim t_s$ occurs mainly for the intrusion beneath the fin for those cases in which Pr is relatively small. In these cases, the intrusion has reached the end of the fin around this time and is being influenced by the transition to a rising plume. The figure therefore supports the scaling (16b) for the initial velocity.

For $Ra_h < Pr^{10}(1 + Pr^{-1/2})^{10}$ and $t > t_s$, the lower intrusion continues to travel under a buoyancy-viscous balance with a velocity scaled by (20b). For the present Ra_h and Pr values, when $t > t_s$ the lower intrusion has usually reached the end of the fin. However, again we are able to validate (20b) using numerical simulations for the case without a fin (see table 1). The scale (20b) remains valid for this case, with Ra_h replaced by Ra. From (20b), using Ra, the velocity scale may be written as $u_{Ivs} \sim \kappa Ra^{9/20}/(h(1 + Pr^{-1/2})^{1/2}(t/t_s)^{1/5})$. In figure 10, the normalized velocity scale $u_{Ivs}h\kappa^{-1}Ra_h^{-9/20}(1 + Pr^{-1/2})^{1/2}$ is plotted against $(t/t_s)^{-1/5}$ for the period past the initial increase in velocity, that is past the peak in the velocities shown in figure 9. Figure 10 shows that for $t > t_s$, the normalized velocity is linearly dependent on $(t/t_s)^{-1/5}$ with a correlation coefficient of 0.915, supporting the scaling (20b). Note that the scaling for $t < t_s$, that is for $(t/t_s)^{-1/5} > 1$ in figure 10, has been confirmed in figure 9 and its associated discussion.

For $Ra_h > Pr^{10}(1 + Pr^{-1/2})^{10}$, large Pr values imply that very large values of Ra_h are required. For example, $Pr = 50$ requires that $Ra_h > O(10^{17})$. Since the Ra_h values in the present simulations are limited to $O(10^9)$ as previously discussed, only numerical results with low Prandtl numbers are applied for the validation of the scales in this flow regime.

In this case the initial intrusion is governed by a buoyancy-viscous balance and has a velocity described by (16b) for the time $t < t_v$, where t_v is given by (15) and $t_v < t_s$. This scale has been verified above. For $t_v < t < t_s$, the inflow to the intrusion remains unsteady but is governed by a buoyancy-inertia balance described by (17b). This scale may be written as $u_{Ig} \sim \kappa Ra_h^{1/3}Pr^{7/6}(1 + Pr^{-1/2})^{2/3}(t/t_v)^{1/2}/h$.

For the purpose of illustrating the transition from the buoyancy-viscous flow regime to the buoyancy-inertial flow regime, figures 11(a) and 11(b) show the
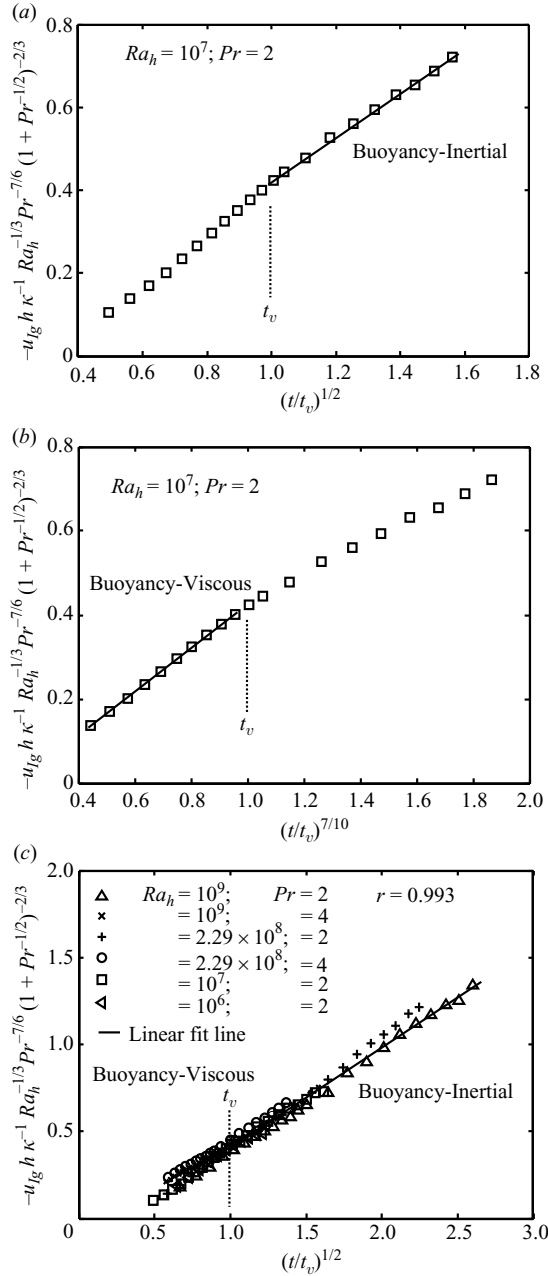
FIGURE 11. Dependence of the front velocity of the lower intrusion on time under the buoyancy-inertial flow regime with an unsteady flow rate for $Ra_h > Pr^{10}(1 + Pr^{-1/2})^{10}$. (a) $-u_{Ig}h/\kappa\, Ra_h^{-1/3}Pr^{-7/6}(1 + Pr^{-1/2})^{-2/3}$ vs. $(t/t_v)^{1/2}$ for $Ra_h = 10^7$ and $Pr = 2$. (b) $-u_{Iv}h/\kappa$ $Ra_h^{-1/3}Pr^{-7/6}(1 + Pr^{-1/2})^{-2/3}$ vs. $(t/t_v)^{7/10}$ for $Ra_h = 10^7$ and $Pr = 2$. (c) $-u_I h/\kappa\, Ra_h^{-5/6}Pr^{-7/6}$ $(1 + Pr^{-1/2})^{-2/3}$ vs. $(t/t_v)^{1/2}$ for different Rayleigh and Prandtl numbers.

dependence of the front velocity of the lower intrusion on time for a typical case of $Ra_h = 10^7$ and $Pr = 2$. Figure 11(a) plots the normalized velocity scale $u_{Ig}hk^{-1}Ra_h^{-1/3}Pr^{-7/6}(1 + Pr^{-1/2})^{-2/3}$ against $(t/t_v)^{1/2}$, with the expectation that for
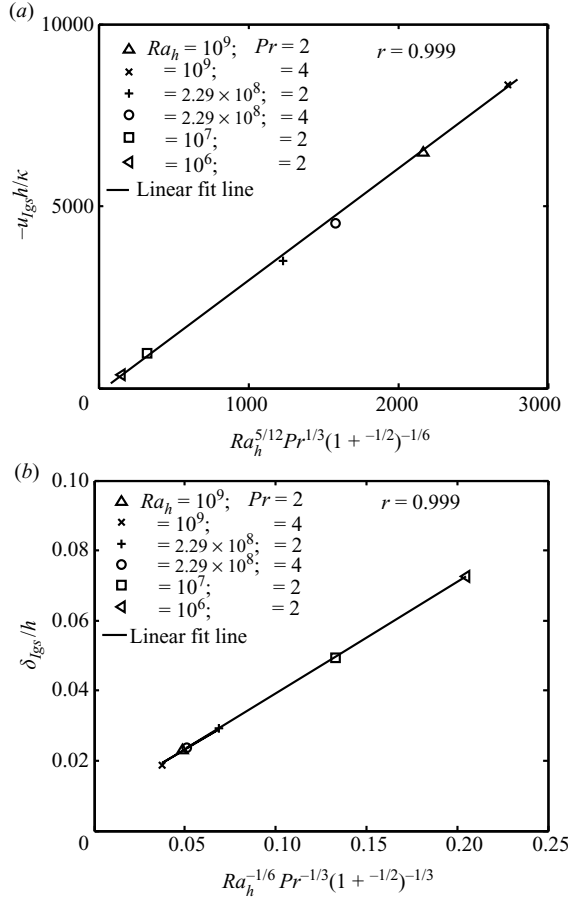
(*a*)

(*b*)

FIGURE 12. (*a*) Front velocity and (*b*) thickness of the lower intrusion at $t \sim t_s$ under the buoyancy-inertial flow regime for $Ra_h > Pr^{10}(1 + Pr^{-1/2})^{10}$.

$t > t_v$ the dependence will be linear, and different to the slope for $t < t_v$. The figure demonstrates this behaviour. Figure 11(*b*) plots the intrusion velocity (scaled by a buoyancy-viscous balance) against $(t/t_v)^{7/10}$, with the expectation that for $t < t_v$ the dependence is linear and different to the slope for $t > t_v$. That is again the case, demonstrating the transition from a buoyancy-viscous balance to a buoyancy-inertia balance around t_v. It is worth noting that the transition process from the buoyancy-viscous flow regime to the buoyancy-inertial flow regime around $t \sim t_v$ is smooth rather than abrupt, as seen in figures 11(*a*) and 11(*b*).

Numerical results for a much wider range of Ra_h and Pr are shown in figure 11(*c*). This figure again plots $u_{Ig} h k^{-1} Ra_h^{-1/3} Pr^{-7/6} (1 + Pr^{-1/2})^{-2/3}$ against $(t/t_v)^{1/2}$. For $t > t_v$ the dependence is approximately linear, with a correlation coefficient of 0.993, supporting the scaling prediction (17*b*).

For $Ra_h > Pr^{10}(1 + Pr^{-1/2})^{10}$ and $t > t_s$, the inflow to the intrusion is steady, with a velocity continuing to be governed by a buoyancy-inertia balance, scaled by (18*b*), at least until viscous influences become important again at time t_g described by (19). Figure 12(*a*) plots the intrusion velocity from this steady part of the flow, normalized by k/h against the non-dimensional parameter $Ra_h^{5/12} Pr^{1/3} (1 + Pr^{-1/2})^{-1/6}$. This shows a clear linear fit with a correlation coefficient of 0.999.

Furthermore, in order to validate the scaling relation (18*a*), we also measured the thickness of the lower intrusion based on the numerical solutions, which is defined as the vertical distance from the lower fin surface to the interior edge of the lower intrusion (at which $T = 0.01$). The numerical results are plotted in figure 12(*b*) for different Ra_h and Pr values. It is seen in this figure that the calculated thickness, normalized by h, has a linear dependence with $Ra_h^{-1/6} Pr^{-1/3} (1 + Pr^{-1/2})^{-1/3}$ with a correlation coefficient of 0.999, as predicted by (18*a*). For times greater than t_g, the velocity scaling for the buoyancy-viscous balance under steady conditions is again relevant.

4.2.2. *Starting plume*

The starting plume ascends under either a buoyancy-inertial balance or a buoyancy-viscous balance, depending on the values of Ra_h, Pr and the fin length. For the present numerical simulations, since the selected fin length is larger than the total distance over which the lower intrusion with an unsteady flow rate travels, that is, $l > l_{gs}$ or l_{vs} (see (22) and (24)), the flow rate to the plume is always constant. Furthermore, since t_{Pv} described by (30) is very small for the present numerical results, only the scaling relations for the starting plume under a buoyancy-viscous balance with a steady flow rate, specified by (32*a*) and (32*b*), are validated in this section.

We treat the horizontal distance from the end of the fin to the interior edge of the plume, as defined above, as the calculated thickness of the starting plume. The calculated thickness, normalized by h, is plotted in figure 13(*a*) against $Ra_h^{-1/4}(1 + Pr^{-1/2})^{-1/6}$ according to (32*a*). A good linear correlation is seen in this figure with a correlation coefficient of 0.998, supporting the scaling prediction (32*a*).

In order to validate the scaling relation (32*b*), we adopt the velocity of the plume front passing through the horizontal plane at $y = 0.5$ as a characteristic velocity scale. Figure 13(*b*) presents the numerical results normalized by κ / h against the scaling prediction $Ra_h^{1/2}(1 + Pr^{-1/2})^{-1/3}$ as suggested by (32*b*). The numerical results are consistent with the scaling relation (32*b*) with a correlation coefficient of 0.989. However, the variation between the cases of different Pr values is also discernible. This could be attributed to the fact that the entrainment of the plume head (see figures 2*b* and 7), which is produced by a strong nonlinear velocity shear of the starting plume, is neglected in the scaling analysis.

4.2.3. *Horizontal thermal flow above the fin*

The scaling relation (39) indicates that the horizontal thermal flow above the fin could be dominated by either a buoyancy-inertial balance or a buoyancy-viscous balance, which is dependent on the values of Ra_h, Pr and the fin length. For the present numerical simulations, since we have either $l \sim l_A$ or $l > l_A$ and, therefore, only the horizontal thermal flow above the fin under a buoyancy-viscous flow regime specified by (36*a*) and (36*b*) is validated.

The vertical distance from the upper fin surface to the interior edge of the horizontal thermal flow is taken as the calculated thickness (note that the interior fluid is isothermal in the early stage of the overall flow development). The calculated thickness, normalized by h, is plotted against the scaling value $(l/h)^{1/4} Ra_h^{-3/16}(1 + Pr^{-1/2})^{-1/8}$ from (36*a*) in figure 14(*a*). Clearly, the numerical results agree with the scaling prediction with a correlation coefficient of 0.997; that is, the thickness of the horizontal fluid layer above the fin under the buoyancy-viscous flow regime is characterized by (36*a*).
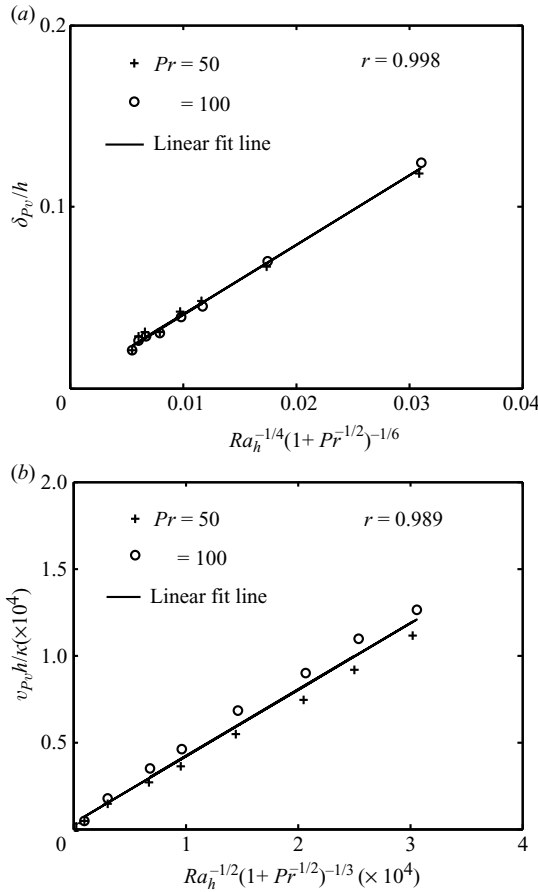
(a)

(b)

FIGURE 13. Front velocity and thickness of the starting plume under the buoyancy-viscous flow regime. (a) δ_{pv}/h vs. $Ra_h^{-1/4}(1+Pr^{-1/2})^{-1/6}$. (b) $v_{pv}h/\kappa$ vs. $Ra_h^{1/2}(1+Pr^{-1/2})^{-1/3}$.

Figure 14(b) shows the calculated velocity normalized by κ/h against the scaling prediction $(l/h)^{-1/4}Ra_h^{7/16}(1+Pr^{-1/2})^{-3/8}$ from (36b). Here, the maximum of the horizontal velocity in the fluid layer above the fin along the vertical line through the fin end is regarded as the calculated velocity. Since the fluid layer above the fin is unstable for the cases with Rayleigh numbers larger than a critical value, the time-averaged velocity is adopted for the validation of the scaling relation. Clearly, the scaling prediction of (36b) is consistent with the calculated results with a correlation coefficient of 0.998.

5. Conclusions

In this paper, the transient natural convection flows around a thin fin placed at the mid height of the sidewall of a differentially heated cavity are investigated using a scaling analysis and direct numerical simulations. A set of scaling relations quantifying the transient natural convection flows around the fin under different dynamic balances has been derived and validated by the corresponding numerical simulations.

The lower intrusion under the fin is initially fed by a time-varying flow rate from the vertical thermal boundary layer, and subsequently by a steady flow rate. The scaling arguments of Huppert (1982) and Maxworthy (1983) are relevant to the unsteady part
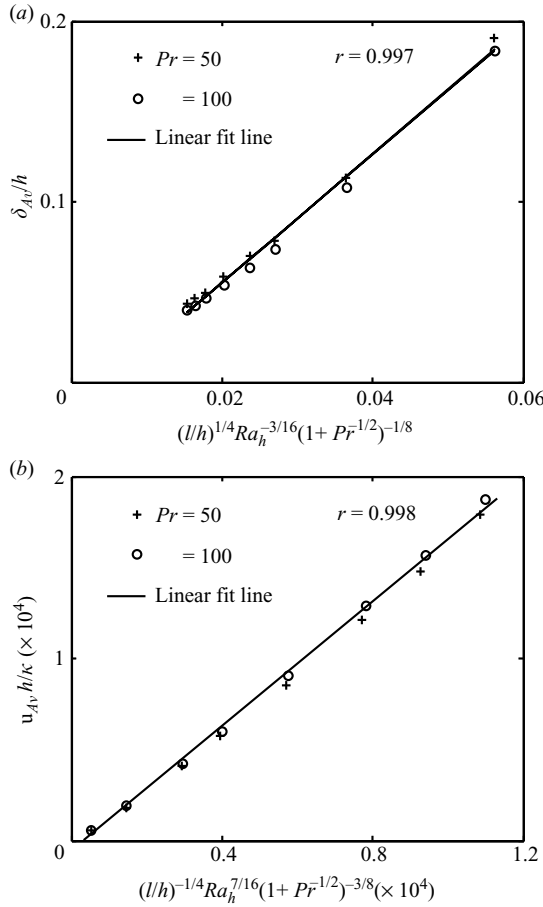
FIGURE 14. Thickness and velocity of the thermal flow above the fin under the buoyancy-viscous flow regime. (a) δ_{Av}/h vs. $(l/h)^{1/4}Ra_h^{-3/16}(1+Pr^{-1/2})^{-1/8}$. (b) $u_{Av}h/\kappa$ vs. $(l/h)^{-1/4}Ra_h^{7/16}(1+Pr^{-1/2})^{3/8}$.

of the flow. Applying these results to the particular flow rate predicted by the vertical boundary-layer scaling reveals that for the case $Ra_h > Pr^{10}(1+Pr^{-1/2})^{10}$, the intrusion travels under a buoyancy-viscous balance if time is sufficiently small. Subsequently, the intrusion is dominated by a buoyancy-inertial balance encompassing the period when the flow rate to the intrusion becomes steady. At much later times, the intrusion travels under a buoyancy-viscous balance again, and its velocity steadily reduces and its thickness increases. For the case of $Ra_h < Pr^{10}(1+Pr^{-1/2})^{10}$, the scaling relations show that a buoyancy-inertial flow regime does not occur and a buoyancy-viscous balance dominates the development of the intrusion during the periods of both increasing flow rate and steady flow rate.

Once the intrusion beneath the fin reaches the end of the fin, it rises as a plume as it is positively buoyant when compared with the ambient, which at this stage remains isothermal at the initial temperature. In some cases, the flow rate from the intrusion to the plume depends on time to certain power. The scaling shows that a critical value of the power is $\gamma_c = 3/2$. If $t \ll t_{Pv}$ for $\gamma > \gamma_c$ or $t \gg t_{Pv}$ for $\gamma < \gamma_c$, the starting plume ascends under the buoyancy-viscous balance, where t_{Pv} is the time for the transition between viscous or inertial dominance in the plume. On the other

hand, if $t \gg t_{Pv}$ for $\gamma > \gamma_c$ or $t \ll t_{Pv}$ for $\gamma < \gamma_c$, a buoyancy-inertial balance dominates the development of the starting plume. For the case of $\gamma = \gamma_c$, if $q_c \ll \nu^{1/2} g\beta\Delta T$, the balance is mainly between the buoyancy and viscous terms, which is independent of time. If $q_c \gg \nu^{1/2} g\beta\Delta T$, the balance is between the buoyancy and inertial terms. For $q_c \sim \nu^{1/2} g\beta\Delta T$, the inertial and viscous terms are comparable.

The horizontal thermal flow above the fin is also described using a simple scaling analysis. The flow above the fin is supplied by a constant flow rate from the intrusion flow beneath the fin, following the entrainment of the rising plume into the vertical boundary layer downstream of the fin. The flow is governed in the initial part of the fin by a buoyancy-advection balance, which, if the fin is sufficiently long, becomes dominated by a buoyancy-viscous balance. The fluid layer above the fin could be unstable if its adverse temperature gradient is larger than a critical value.

The scaling relationships describe very complex interactions between the vertical boundary layer development, the intrusion beneath the fin, the initial rising plume emanating from the end of the fin, and the fully developed horizontal flow above the fin. Although the scaling relations are relevant to a wide range of parameter values for the individual flows, only a relatively small subset of the flow regimes may be achieved in the context of the flows in the cavity with a fin. Consequently, the validation by the numerical simulations is necessarily limited.

Furthermore, it is worth noting again that the interior fluid in the cavity gradually becomes stratified after the intrusion from the opposing sidewall strikes the finned sidewall but remains isothermal at the earlier stage (refer to Xu *et al.* 2009). Consequently, the present scaling relations are not applicable to the flows around the fin at the much later time scale when the cavity flows have reached steady states. In addition, since the dynamic mechanisms of the thermal boundary layer flow are different between $Pr > 1$ and $Pr < 1$ (Patterson & Imberger 1980; Lin & Armfield 2005), the present scaling relations are applicable only to the cases of $Pr > 1$ rather than those of $Pr < 1$, for which multiple steady states of the cavity flow may exist (see Gelfgat, Bar-yoseph & Yarin 1999).

With the above-mentioned limitations, the numerical results in general support the scaling results presented, leading to an understanding of how this complex early flow develops. A separate investigation is required for the development of the longer time scale flow as the interior becomes stratified, leading ultimately to a cavity-wide steady state.

REFERENCES

ARMFIELD, S. W. & JANSSEN, R. J. A. 1996 A direct boundary-layer stability analysis of steady-state cavity convection flow. *Intl J. Heat Fluid Flow* **17**, 539–546.

ARMFIELD, S. W. & PATTERSON, J. C. 1992 Wave properties of natural-convection boundary layers. *J. Fluid Mech.* **239**, 195–211.

BACHELOR, G. K. 1954 Heat transfer by free convection across a closed cavity between vertical boundaries at different temperatures. *Quart. Appl. Math.* **12**, 209–233.

BEJAN, A. 1983 Natural convection heat transfer in a porous layer with internal flow obstructions. *Intl J. Heat Mass Transfer* **26**, 815–822.

BILGEN, E. 2005 Natural convection in cavities with a thin fin on the hot wall. *Intl J. Heat Mass Transfer* **48**, 3493–3505.

CAMPBELL, I. H., GRIFFITHS, R. W. & HILL, R. I. 1989 Melting in an archaean mantle plume: heads it's basalts, tails it's komatiites. *Nature* **339**, 697–699.

DIDDEN, N. & MAXWORTHY, T. 1982 The viscous spreading of plane and axisymmetric gravity currents. *J. Fluid Mech.* **121**, 27–42.

ELDER, J. W. 1965a Laminar free convection in a vertical slot. *J. Fluid Mech.* **23**, 77–98.

ELDER, J. W. 1965b Turbulent free convection in a vertical slot. *J. Fluid Mech.* **23**, 99–111.

FREDERICK, R. L. & VALENCIA, A. 1989 Heat transfer in a square enclosure with a partition attached to its cold wall. *Intl Commun. Heat Mass Transfer* **16**, 347–354.

GELFGAT, A. YU 2007 Stability of convective flows in cavities: solution of benchmark problems by a low-order finite volume method. *Intl J. Numer. Meth. Fluids* **53**, 485–506.

GELFGAT, A. YU, BAR-YOSEPH, P. Z. & YARIN, A. L. 1999 Stability of multiple steady states of convection in laterally heated cavities. *J. Fluid Mech.* **388**, 315–334.

GILL, A. E. 1966 The boundary-layer regime for convection in a rectangular cavity. *J. Fluid Mech.* **26**, 515–536.

GOLDSTEIN, R. J. & BRIGGS, D. G. 1964 Transient free convection about vertical plates and cylinders. *J. Heat Transfer* **86**, 490–500.

HUPPERT, H. 1982 The propagation of two-dimensional and axisymmetric viscous gravity currents over a rigid horizontal surface. *J. Fluid Mech.* **121**, 43–58.

HYUN, J. M. 1994 Unsteady buoyant convection in an enclosure. *Adv. Heat Transfer* **24**, 277–320.

JANSSEN, R. J. A. & ARMFIELD, S. W. 1996 Stability properties of the vertical boundary layers in differentially heated cavities. *Intl J. Heat Fluid Flow* **17**, 547–556.

JANSSEN, R. J. A. & HENKES, R. A. W. M. 1995 Influence of Prandtl number on instability mechanisms and transition in a differentially heated square cavity. *J. Fluid Mech.* **290**, 319–344.

JOSHI, Y. & GEBHART, B. 1987 Transition of transient vertical natural-convection flows in water. *J. Fluid Mech.* **179**, 407–438.

KAMINSKI, E. & JAUPART, C. 2003 Laminar starting plumes in high-Prandtl-number fluids. *J. Fluid Mech.* **478**, 287–298.

LEI, C. & PATTERSON, J. C. 2002 Unsteady natural convection in a triangular enclosure induced by absorption of radiation. *J. Fluid Mech.* **460**, 181–209.

LIN, W. & ARMFIELD, S. W. 2005 Unsteady natural convection on an evenly heated vertical plate for Prandtl number $Pr < 1$. *Phys. Rev.* E **72**, 066309.

LIN, W., ARMFIELD, S. W. & PATTERSON, J. C. 2007 Cooling of a $Pr < 1$ fluid in a rectangular container. *J. Fluid Mech.* **574**, 85–108.

LIN, W., ARMFIELD, S. W., PATTERSON, J. C. & LEI, C. 2009 Scalings with the Pr variation for unsteady natural convection boundary layers of $Pr > 1$ fluids under isothermal heating. *Phys. Rev.* E **79**, 066313.

LIST, E. J. 1982 Turbulent jets and plumes. *Ann. Rev. Fluid Mech.* **14**, 189–212.

MAHAJAN, R. L. & GEBHART, B. 1978 Leading edge effects in transient natural convection flow adjacent to a vertical surface. *J. Heat Transfer* **100**, 731–733.

MAXWORTHY, T. 1983 Gravity currents with variable inflow. *J. Fluid Mech.* **128**, 247–257.

MOSES, E., ZOCCHI, G. & LIBCHABER, A. 1993 An experimental study of laminar plumes. *J. Fluid Mech.* **251**, 581–601.

NAG, A., SARKAR, A. & SASTRI, V. M. K. 1993 Natural convection in a differentially heated square cavity with a horizontal partition plate on the hot wall. *Comput. Methods Appl. Mech. Engng* **110**, 143–156.

NAG, A., SARKAR, A. & SASTRI, V. M. K. 1994 Effect of thick horizontal partial partition attached to one of the active walls of a differentially heated square cavity. *Numer. Heat Transfer* A **25**, 611–625.

OOSTHUIZEN, P. L. & PAUL, J. T. 1985 Free convection heat transfer in a cavity fitted with a horizontal plate on the cold wall. *Adv. Enhanced Heat Transfer* **43**, 101–107.

OSTRACH, S. 1988 Natural convection in enclosures. *J. Heat Transfer* **110**, 1175–1190.

PATTERSON, J. C. & ARMFIELD, S. W. 1990 Transient features of natural convection in a cavity. *J. Fluid Mech.* **219**, 469–497.

PATTERSON, J. C., GRAHAM, T., SCHÖPF, W. & ARMFIELD, S. W. 2002 Boundary layer development on a semi-infinite suddenly heated vertical plate. *J. Fluid Mech.* **453**, 39–55.

PATTERSON, J. C. & IMBERGER, J. 1980 Unsteady natural convection in a rectangular cavity. *J. Fluid Mech.* **100**, 65–86.

POULIKAKOS, D. & BEJAN, A. 1983 The fluid dynamics of an attic space. *J. Fluid Mech.* **131**, 251–269.

SHAKERIN, S., BOHN, M. & LOEHRKE, R. I. 1988 Natural convection in an enclosure with discrete roughness elements on a vertical heated wall. *Intl J. Heat Mass Transfer* **31**, 1423–1430.

SHI, X. & KHODADADI, J. M. 2003 Laminar natural convection heat transfer in a differentially heated square cavity due to a thin fin on the hot wall. *J. Heat Transfer* **125**, 624–634.

SHLIEN, D. J. 1976 Some laminar thermal and plume experiments. *Phys. Fluids* **19**, 1089–1098.

TASNIM, S. H. & COLLINS, M. R. 2004 Numerical analysis of heat transfer in a square cavity with a baffle on the hot wall. *Intl Commun. Heat Mass Transfer* **31**, 639–350.

TURNER, J. S. 1962 The 'starting plume' in neutral surroundings. *J. Fluid Mech.* **13**, 356–368.

XU, F., PATTERSON, J. C. & LEI, C. 2005 Shadowgraph observations of the transition of the thermal boundary layer in a side-heated cavity. *Exp. Fluids* **38**, 770–779.

XU, F., PATTERSON, J. C. & LEI, C. 2006 Experimental observations of the thermal flow around a square obstruction on a vertical wall in a side-heated cavity. *Exp. Fluids* **40**, 363–371.

XU, F., PATTERSON, J. C. & LEI, C. 2008 An experimental study of the unsteady thermal flow around a thin fin on a sidewall of a differentially heated cavity. *Intl J. Heat Fluid Flow* **29**, 1139–1153.

XU, F., PATTERSON, J. C. & LEI, C. 2009 Transition to a periodic flow induced by a thin fin on the sidewall of a differentially heated cavity. *Intl J. Heat Mass Transfer* **52**, 620–628.